Development of hybrid 3D-printed structure with aligned drug-loaded fibres using in-situ custom designed templates

Journal of Drug Delivery Science and Technology 88 (2023) 104921

Contents lists available at ScienceDirect

Journal of Drug Delivery Science and Technology

journal homepage: www.elsevier.com/locate/jddst

Development of hybrid 3D-printed structure with aligned drug-loaded fibres using in-situ custom designed templates

Kirsty Muldoon [a], Yu Feng [a], Thomas Dooher [b], Caolan O'Connor [a], Baolin Wang [c], Hui-Min David Wang [d], Zeeshan Ahmad [e], James McLaughlin [a], Ming-Wei Chang [a,*]

[a] Nanotechnology and Integrated Bioengineering Centre (NIBEC), School of Engineering, Ulster University, York Street, Belfast, BT15 1AP, UK
[b] Northern Ireland Advanced Composites and Engineering Centre (NIACE), Airport Road, Belfast, BT3 9EF, UK
[c] Hebei Key Laboratory of Bioelectromagnetics and Neuroengineering, School of Health Sciences and Biomedical Engineering, Hebei University of Technology, 300132, Tianjin, China
[d] Graduate Institute of Biomedical Engineering, National Chung Hsing University, Taichung, 402, Taiwan
[e] Leicester School of Pharmacy, De Montfort University, Leicester, UK

ARTICLE INFO

Keywords:
Aligned fibres
Electrospinning
Drug release
Custom electrodes
Additive manufacturing

ABSTRACT

Fibre alignment technology is crucial in various emerging applications, such as drug delivery systems, tissue engineering, and scaffold fabrication. However, conventional methods have limitations when it comes to incorporating aligned fibres into 3D printed structures in situ. This research demonstrates the use of custom-designed templates made with conductive ink to control the alignment of drug-loaded polymer fibres on a 3D printed microscale structure. Three different geometries were designed, and the effects of the template on fibre diameter and pattern were investigated. The hybrid structure demonstrated successful control of aligned fibres on printed structures using grounded conductive ink geometric electrodes, as confirmed by SEM. All three custom-designed templates presented unique geometric alignments and fibre diameters of around 1 μm. Additionally, the different collector shapes had an impact on the distribution of fibre diameters. FTIR and EDX analyses concluded that the drug was effectively encapsulated throughout the fibres. In-situ deposition of fibres onto the 3D printed structure enhanced the mechanical properties, and water contact angle results showed that the hybrid structure transitioned to a hydrophilic state with the addition of fibres. A drug delivery study confirmed that the hybrid structure functions as a steady release system, following a Korsmeyer-Peppas kinetic release model. TGA results indicated that the samples are thermally stable, and DSC analysis concluded that the samples were homogeneously produced. The results obtained from the hybrid structures provide a novel mechanism for integrating aligned fibres and 3D printed structures for development in fields such as biomedical engineering, regenerative medicine, and advanced manufacturing.

1. Introduction

Electrospinning (ES) is a solvent-based fabrication method that involves setting up a voltage supply, a syringe pump, a spinneret, and a conductive collector [1,2]. The technique generates fibres ranging from nanometers to a few micrometers when high voltage is applied to a liquid droplet [3–5]. The liquid becomes charged and counteracts surface tension when electrostatic repulsion occurs, resulting in tangential stress that stretches the droplet into a liquid stream known as the Taylor cone [6]. Initially, the jet produced from the electrically induced liquid stream extends in a straight line, followed by vigorous whipping motions caused by bending instabilities. As the jet stretches, it solidifies, leading to the deposition of fibres on the grounded collector. The electrostatic stress overcomes the surface tension at the cones tip, causing ink ejection [7].

Aligned fibres have gained interest in many sectors, including electronics, biomedical applications, and composites. Unique features such as enhanced mechanical properties, faster charge transport, and a more regulated spatial structure are associated with aligned electrospun fibers [8,9]. Often, the set-up needs additional apparatus that can alter the trajectory of the fibres, typically in the form of the collector. Methods of aligning electrospun fibres include gap [10], rotational [11], magnetic

* Corresponding author.
E-mail address: m.chang@ulster.ac.uk (M.-W. Chang).

https://doi.org/10.1016/j.jddst.2023.104921
Received 2 July 2023; Received in revised form 30 August 2023; Accepted 2 September 2023
Available online 7 September 2023

[12], centrifugal [13], near-field [14] and post-drawing [15], and centrifugal [16] electrospinning. However, these techniques have limitations in terms of design and are typically limited to a single degree of alignment. Another limitation of conventional aligned electrospinning is that dynamic methods produce weak and brittle fibres. Therefore, there is a significant need for an electrospinning technology capable of fabricating stable fibres with the flexibility to adjust the degree of alignment.

In recent years, 3D printing has become a more common method of fabrication due to its capability for complex geometry, low manufacturing cost and rapid production time [17–20]. Similar to aligned fibre electrospinning, there are many fabrication methods of 3D printing, such as extrusion [21], lithography [22] and inkjet [23]. Hot melt extrusion (HME) based 3D printing applies high pressure to thermoplastic polymers at their optimal melting point [24]. This technique is particularly beneficial in biomedical applications due to its biomaterial diversity and layer-by-layer approach, which enables the production of sophisticated structures with functional relevance [21]. HME offers advantages as an additive manufacturing technique over other methods due to its cost effectiveness, solvent free process and continuity [25]. The 'green' manufacturing process is capable of preparing amorphous drug-polymer formulations and co-amorphous formulations in a larger scale [26]. Issues of oral bioavailability of drugs with poor water solubility can be overcome through HME due to its flexibility and production of distinct dosage forms heavily implemented for various drug delivery applications [27]. HME is applicable to many biomedical applications such as scaffolds [28], tissue engineering [29] and drug delivery systems [30]. Its resolution scale is larger and on the microscale, compared to electrospinning which can achieve the nano-scale. Due to limitations of 3D printers suitable for biomedical device requirements, it is becoming more common within research and industry to combine multiple 3D printing technologies to innovate complex structures.

In this study, we demonstrate the benefits of coupling HME with electrospinning to manufacture a hybrid structure with sustained drug release capabilities, showcasing the controlled release of drugs from aligned fibres. Firstly, a structure is 3D printed using HME to perform as the substrate to collect aligned fibres using a formulation consisting of polycaprolactone, iron oxide nanoparticles and drug according to previous work [24]. Tetracycline hydrochloride, an FDA-approved antibiotic commonly used to treat infections, is selected as the model drug and is encapsulated within biodegradable polycaprolactone (PCL). The alignment of drug-loaded fibres is controlled by manipulating the electric field using custom-designed grounded collectors. This research presents a novel ES technique that offers advantages as the custom design templates provide the flexibility to model various alignment geometries.

2. Materials and methods

2.1. Materials

Polycaprolactone powder (PCL, Mw = 50,000 $gmol^{-1}$) was purchased from Poly-science Europe (Germany). PCL pellets (Mn 80,000), Tetracycline Hydrochloride (TH, Mw = 480.90 gmol−1), Dichloromethane (DCM) and Dimethylformamide (DMF) was purchased from Sigma Aldrich (USA). Iron oxide nanoparticles (IONP) (Fe_3O_4, particle size <63 nm) were obtained from Inoxia chemicals (UK).

2.2. Electrospinning solution preparation

An electrospinning solution of 9 wt/v% PCL was prepared by dissolving PCL in a 4:1 ratio of DCM to DMF. The solution was mixed using a magnetic stirrer at 500 rpm until complete dissolution of PCL pellets. A 0.75 wt/v% of tetracycline hydrochloride was added to the solution and magnetically stirred at 500 rpm until complete dissolution. The solution preparation process was conducted entirely at room temperature.

2.3. 3D printed substrate fabrication

A 20 mm by 20 mm substrate consisting of 4 layers of lines in an alternating 0°/90°/0°/90° pattern was prepared by 3D Bioplotter (EnvisionTEC, Gladbeck, Germany). 1 mm spacing between strands was selected as the pattern so that the vertical and horizontal extrusions created a regular porous structure. A stainless-steel syringe with 22-gauge needle tip was loaded with 98.5 wt% PCL powder, 0.5 wt% Fe_3O_4 and 1.0 wt% TH. The high temperature syringe was heated to 130 °C and the pressure and printing speed was set to 6 bar and 1.5 mm/s respectively. Printing parameters and pattern were set using Visual Machine 2.8.115 software (EnvisionTEC, Gladbeck, Germany).

2.4. Electrospinning set-up and template design

The electrospinning equipment in Fig. 1 for aligned fibres includes a syringe pump (Cole Palmer, UK), a high voltage supply (Heinzinger, Germany), 5 mL plastic syringes (Terumo, UK), silicon tubing and a metallic blunt end needle tip with an outer diameter of 1.8 mm and an inner diameter of 1.4 mm. The custom designed templates were formed using an insulating collector and conductive ink (Bare Conductive) to construct a parallel, square bracket and circular electrode designs with distances of 2.0, 2.5, 3.0 and 3.5 cm. The width of the conductive ink designs was approximately 1 mm. The length was 25 mm for parallel and square bracket, and for circle the conductive ink was 3 mm in width from the inner diameter to the outer diameter The needle tip was positioned at a height of 10 cm from the grounded collector, and an applied voltage of 8.5 kV was supplied to the needle tip with a collection time of 3 min and a flow rate of 0.35 ml/h. The electrospinning parameters remained constant for all samples under the stable cone-jet mode.

2.5. Fibre sizes and fourier transform infrared spectroscopy

Alignment and fibre topography were analysed using Scanning Electron Microscopy (SEM) on all samples with varying geometries and their respective distances. A Hitachi SU5000 field emission instrument (Hitachi, Europe) was used in high vacuum with a secondary electron (SE) signal. ImageJ software was used to conduct measurements on 50 randomly selected fibres of varying distances to calculate the average fibre diameter and standard deviation. Energy dispersive X-ray (EDX) analysis was conducted on the electrospun 3D printed sample to identify the elements present on the surface, particularly in the fibres to observe their dispersion via the electrospinning process. Hitachi SU5000 field emission instrument (Hitachi, Europe) was employed with an accelerating voltage of 10 kV to form an elemental mapping of the surface.

Fourier transform infrared (FTIR) spectroscopy was employed to obtain a spectrum of tetracycline hydrochloride in powder form, with KBr serving as the background. Attenuated total reflectance (ATR-FTIR) was performed on PCL pellets and the 3D printed structure containing electrospun fibres. This allowed for the detection and comparison of the chemical composition of the individual components before and after the electrospinning process. The analysis was conducted in transmission mode using Varian 640-IR (UK) at a resolution of 4 cm^{-1}, recording within a wave range of 400–4000 cm^{-1} with 30 scans per sample.

2.6. Surface water contact angle

The surface wettability of electrospun drug loaded PCL fibres on 3D printed structure was studied using water contact angle (WCA) measurements using an optical contact angle meter CAM 200 (KSV instruments LTD, Helsinki, Finland). WCA measurements were performed on substrates with parallel, square bracket, and circularly aligned fibres. A substrate containing no fibres was also included for comparison. Measurements were performed with a 10 μL drop size, with three repetitions performed for each sample. Each measurement included a left

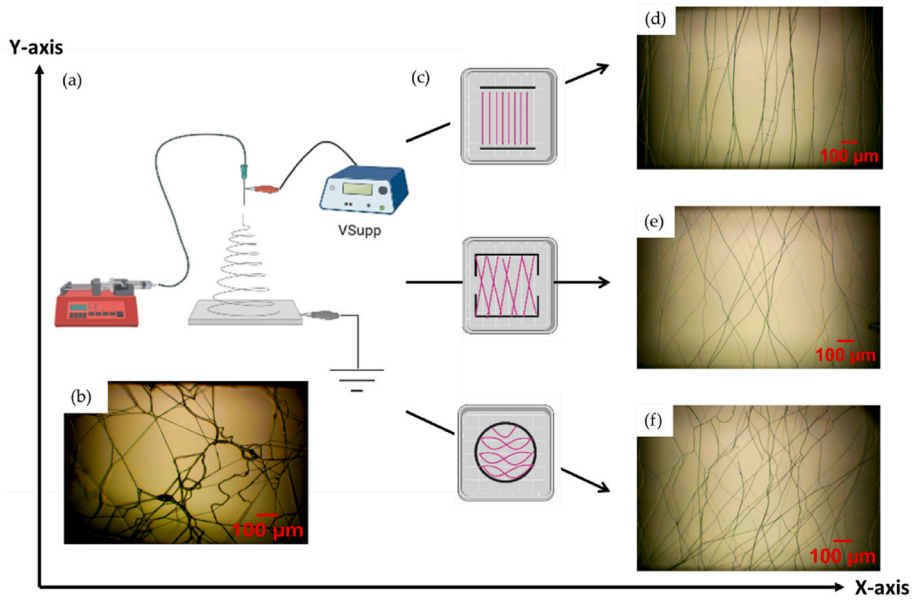

Fig. 1. Schematic representation of (a) electrospinning set-up, (b) optical microscopy image showing random fibre deposition, (c) substrate with conductive ink electrodes and their corresponding fibre alignment, (d) parallel geometry, (e) square bracket geometry, and (f) circular geometry.

and right WCA, and the average value was calculated from these measurements to determine the overall WCA per sample.

2.7. Mechanical testing

To assess the impact of incorporating electrospun fibres aligned with three different geometries on the mechanical properties of the structure, tensile testing was performed using an Instron 5500R machine (Instron, Norwood, MA, USA). A load cell with a capacity of 500 N was employed, and the testing was carried out at a crosshead speed of 10 mm/min. The Bluehill 2 software was utilized to collect the data on tensile stress (MPa) versus tensile strain (%).

2.8. Thermogravimetric analysis (TGA) and differential scanning colorimetry (DSC)

As the substrate used to collect drug loaded electrospun fibres was manufactured by hot melt extrusion, the thermal behaviour of the hybrid scaffold, substrate and fibres were examined using SDT Q600 (TA instruments, USA). Test results were obtained from ambient temperature to 1000 °C at a heating rate of 10 °C per minute under flow of nitrogen gas. The results were analysed using Universal Analysis software (TA instruments, USA). Differential scanning colorimetry (DSC) was conducted under a flowing nitrogen atmosphere using DSC 25 (TA instruments, USA) to characterize thermal characteristics. Prepared samples of the hybrid structure, substrate and fibres were weighed and placed in a hermetic aluminium pan. The reference pan used was an empty sealed aluminium hermetic pan of the same type as the sample pan. A heat-cool-heat cycle from −90 °C to 250 °C with a 10 °C per minute heating rate and a 5 °C per minute cooling rate. Analysis was carried out using TRIOS software (TA instruments, USA).

2.9. Drug release study

Release behaviour of tetracycline hydrochloride from drug loaded fibres in a hybrid 3D structure was studied over a period of 10 days. UV–Vis spectrophotometry was performed using Lambda 365 (PerkinElmer, Buckinghamshire, UK) to form a standard curve of concentration versus absorbance. A characteristic peak for UV–Vis of TH was determined at 343 nm according to previous work [31]. The standard curve was formed using a series of concentrations of TH in PBS ranging from 1.25 to 20%. Three replicates of each geometry were produced for the drug release study, all of which were immersed in 40 ml of PBS (pH = 7.2–7.6) (Sigma, UK) and incubated at 37 °C 1 ml aliquots were taken every 24 h and replaced with 1 ml of PBS medium. The standard curve of absorbance vs concentration was used to determine the concentration of TH release in mg/ml. A cumulative release graph in mg/ml across 10 days was produced by adding the amount of drug released in mg/ml at each time point to the total amount of drug released from the beginning of the study in mg/ml. Cumulative release (%) was also performed by scaling up mg/ml to mg/40 ml as the sample was immersed in 40 ml PBS. The following equation, eq (1), was used to determine cumulative release (%) [32]:

$$Cumulative\ release\ (\%) = \frac{Dt}{Ds}\ x\ 100 \tag{1}$$

where *Dt* is the amount of drug present in mg/ml at time point *t*, and *Ds* is the final amount of drug present in the sample at the end of the study in mg/ml. Mathematical modelling of kinetic drug release was performed on three alignment geometries using KinetDS 3.0 software.

The Korsmeyer-Peppas equation, Eq (2), was used to fit the cumulative percentage release data. Where M_t/M_∞ is the permeated drug, *t* is time, *K* is the transport constant and *n* is the transport exponent [33].

$$\frac{M_t}{M_\infty} = K \times t^n \tag{2}$$

2.10. Simulation

To investigate the impact of different substrate templates on the distribution of electrospun fibers, the Ansys software was utilized to simulate the electric field using finite element methods. The electrostatic solution type in Maxwell 3D was employed to simulate and solve the electric field distribution based on the designed geometric model and physical properties. The substrate and three distinct templates were developed with relative permittivity values of 2.25 and 11.9, respectively, while the nozzle possessed a relative permittivity of 1. The simulation region was defined for the nozzle, substrate, and template system, and the distribution of electric field strength was simulated. The simulation process utilized the same theoretical model, with an applied voltage of 8.5 kV at the nozzle, and incorporated three different

template shapes and sizes to assess their influence on the electric field strength distribution.

3. Results and discussion

3.1. Fibre alignment using custom designed electrodes

A non-modified electrospinning set-up is shown in Fig. 1(a) consisting of a voltage supply, grounded electrode, and a syringe pump. The result of fibre orientation from this set-up is illustrated in an OM image in Fig. 1(b). The fibres are randomly deposited on the grounded electrode as the electric field is well distributed and fibres are trajected from the needle orifice in a whipping motion [34]. The grounded electrode, as depicted in Fig. 1(c), has been designed in this study using conductive ink to create three different geometries: parallel electrodes, square bracket electrodes, and circular electrodes. These geometries result in three distinct forms of aligned fibres, as illustrated in Fig. 1(d–f). The results obtained with custom-designed electrodes demonstrate controllable axial alignment for both square bracket and circular electrodes, whereas alternative alignment strategies yield uniaxial alignment [35, 36].

3.2. Parallel electrodes

Parallel electrodes, formed from conductive ink outside the 3D printed hybrid structure, result in uniaxial alignment of fibres due to the manipulation of the electric field caused by the conductive ink. The gap distance in the custom-designed electrodes plays a crucial role in determining the size of the fibres deposited on the structure. Fig. 2(b) shows a high magnification SEM image of Fig. 2(a), illustrating the aligned fibres and demonstrating the impact of fibre distribution on the increase in gap distance shown in Fig. 2(c). The average fibre diameters were measured as 2.5 μm, 2.0 μm, 1.6 μm, and 1.3 μm for gap distances of 2 cm, 2.5 cm, 3 cm, and 3.5 cm, respectively. Increasing the gap distance results in a decrease in the average fibre diameter, as the greater distance causes the fibres to stretch across the insulating collector, resulting in smoother and finer fibres. The alignment of fibres occurs regardless of the position of the 3D printed structure, indicating the significance of the electric field in positioning the fibres over the gaps in the substrate. This control over fibre deposition demonstrates that a printed structure is not required for fibre alignment, but it highlights the flexibility to generate in-situ aligned fibres on printed structures. Gap distances of 2 cm and 2.5 cm showed the largest variations in fibre diameter, which can be attributed to the shorter conductive pathways formed by these distances, resulting in aligned fibres with the largest diameter. Standard deviations in fibre diameter measurements may appear elevated due to electric field variations across the electrode stemming from the geometry presented in Fig. 2(f) as the distance increases, resulting in a minor difference of ~2 μm.

3.3. Square bracket electrodes

The square bracket electrodes exhibit differences in fibre diameter and alignment compared to the custom-designed parallel geometry template. Fig. 2(d) still demonstrates a dominant alignment along the y-axis, but there is a variation in the alignment angle due to the complexity

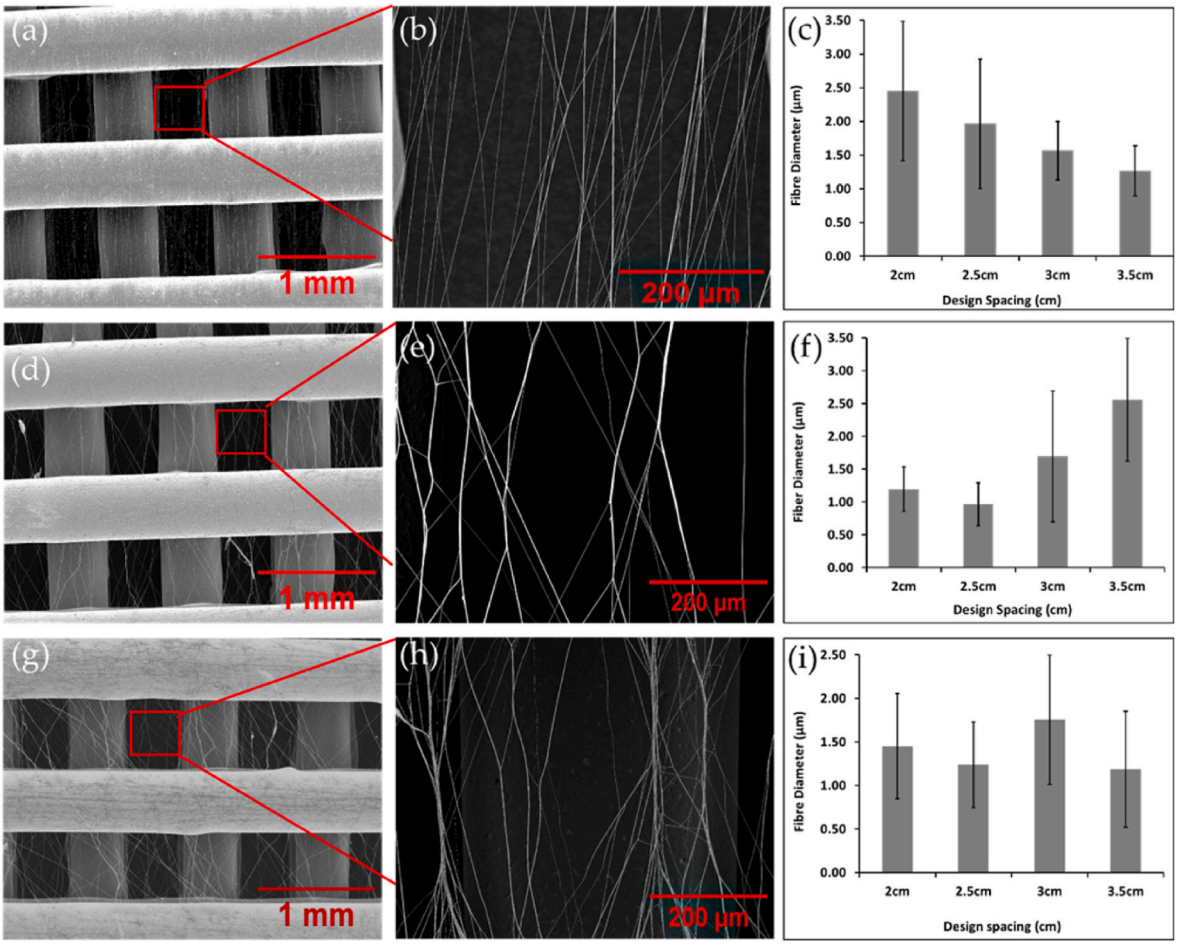

Fig. 2. Scanning Electron Microscopy (SEM) images of aligned fibres and their corresponding average fibre diameter distribution, showcasing the effect of increasing design spacing for parallel electrode (a–c), square bracket electrode (d–f), and circular electrode (g–i).

introduced by the geometry. Consequently, the path of conductive ink and electric field has influenced the distribution of fibre diameters, as shown in Fig. 2(d–f) with different trends compared to Fig. 2(a–c). The average fibre diameters were calculated as 1.2 μm, 0.8 μm, 1.7 μm, and 2.6 μm for gap distances of 2 cm, 2.5 cm, 3 cm, and 3.5 cm, respectively. This fibre diameter range is suitable for drug delivery applications, as fibres with diameters around 1 μm exhibit high surface area, efficient mass transport, and interconnected porosity [37]. The fibre diameter can be tailored for specific applications by adjusting the concentration of the electrospinning solution or modifying the electrospinning process parameters. The angles introduced in the upper and lower regions of the square brackets impact the alignment angle, as these regions have shorter conductive paths than others. Fibres from the needle tend to deposit where the electric field strength is highest, where the flow of electrons has the shortest distance to travel. In contrast to the previous data for the parallel template, the fibre diameter increases when the gap spacing increases from 2.5 cm to 3 cm.

3.4. Circular electrodes

Rope-like fibres with a twisting appearance were formed using circular electrodes, as shown in Fig. 2(g–i). Zhang et al. previously conducted a study to produce twisted electrospun fibres using a rotary funnel collector [38], but the phenomenon observed in this study presents a unique technique for achieving such fibrous structures. Compared to Fig. 2(a), there is a difference in the degree of alignment. Although fibres predominantly align in the y-direction, they appear to be deposited at an angle. Therefore, the circular geometry has influenced the direction of fibre alignment. At higher magnification (Fig. 2(h)), the fibres are observed to twist around each other, forming a rope-like structure not observed previously. This can be attributed to the geometry's impact on the electric field. Fig. 2(i) demonstrates the effect of increasing the distance of the circular electrode on fibre diameter. Increasing the distance from 2 cm to 3.5 cm resulted in average fibre diameters of 1.5 μm, 1.2 μm, 1.8 μm, and 1.2 μm, respectively. There is a general decreasing trend of fibre diameter with increasing circular electrode diameter, except for the 3 cm geometry. However, as all circular geometries investigated exhibited a large standard deviation, it can be concluded that the circular geometry shows a significant variation in fibre diameter regardless of the electrode distance. This geometry exhibits the least control over alignment and fibre diameter compared to the parallel and square bracket geometries studied. The rate of solvent evaporation plays a role in varying fibre diameter. Rapid solvent evaporation, accompanied by jet stretching under an electric field, can cause instabilities that affect fibre diameter and structure [39]. Comparing the fibre diameter distribution across all geometries, it can be concluded that a spacing of 2 cm is suitable for testing the effect of alignment on drug release profile, mechanical testing, and water contact angle (WCA). This geometric spacing exhibits the least fluctuation in fibre diameter across geometries and has the smallest standard deviation range, thereby excluding fibre diameter as a variable influencing the results and allowing the geometry of alignment to be the independent variable.

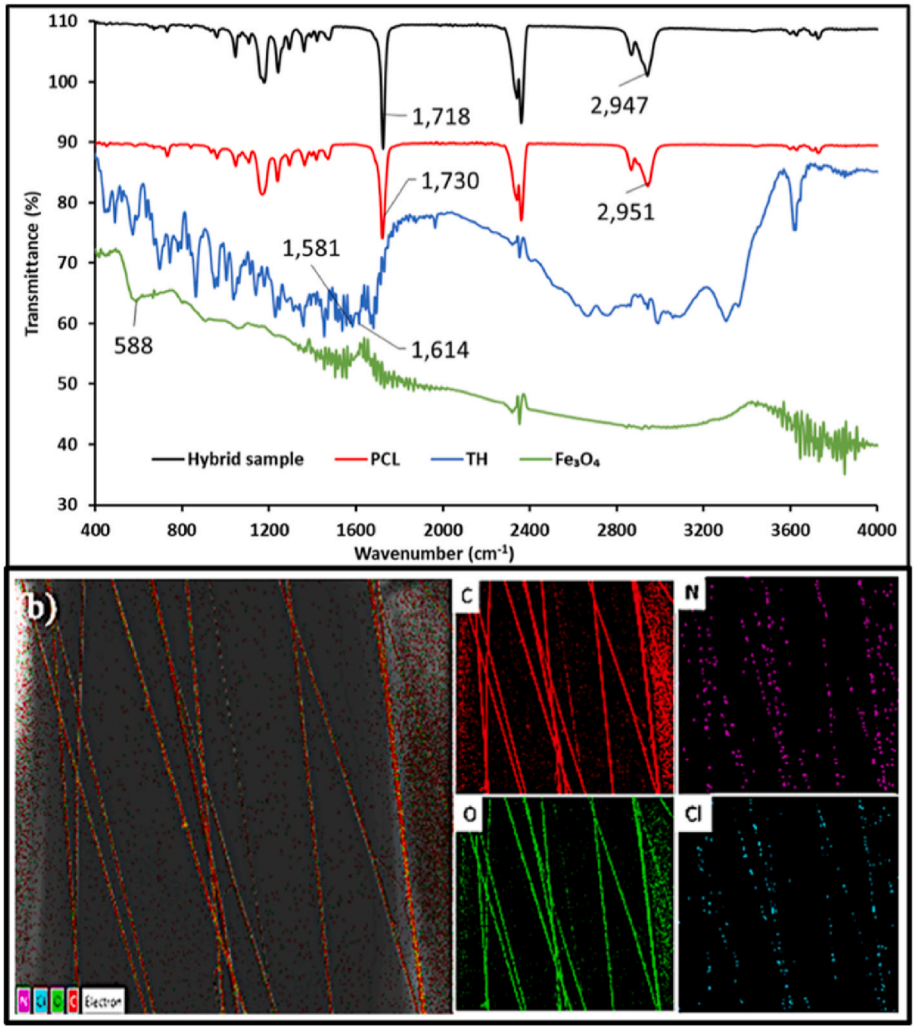

Fig. 3. FTIR spectrum of PCL, TH and 3D printed hybrid structure (a), and EDX mapping of 3D printed hybrid structure (b).

3.5. Elemental characterisation

Fourier Transform Infrared (FTIR) analysis was conducted on the hybrid sample, as well as each component comprising the sample. Fig. 3 (a) displays the characteristic peak of Fe_3O_4 at 588 cm^{-1}, corresponding to the Fe–O bond [40]. However, this peak is not observed in the hybrid sample spectrum. This absence can be attributed to FTIR being a surface characterization technique, and since the Fe_3O_4 nanoparticles are embedded within the substrate of the sample, they cannot be detected on the surface, which is composed of TH-loaded polymer fibres. It is important to note that the presence of Fe_3O_4 nanoparticles within the sample arises from their random distribution in minute quantities. This randomness influences the probability of their occurrence on the surface or their encapsulation within the samples. This observation is in line with previous studies that demonstrated the random dispersion of nanoparticles within the polymer matrix [24].Distinctive peaks for TH have been reported at 1579 cm^{-1} and 1613 cm^{-1}, which are associated with the C═O ring and NH2 amide bond of TH [41]. The spectrum for TH exhibits two characteristic peaks at 1581 cm^{-1} and 1614 cm^{-1}, aligning with the reported values. However, these peaks are absent in the transmittance spectrum of the hybrid sample due to the encapsulation of the drug within the polymer during the electrospinning process. This is supported by the PCL spectrum, which aligns with the hybrid sample spectrum, indicating that PCL is detectable on the surface while TH is encapsulated within the polymer. The spectra of both PCL and the hybrid sample are highly similar, displaying strong characteristic peaks at comparable wavelengths. The peaks at 2951 cm^{-1} and 1730 cm^{-1} are attributed to CH2 and carbonyl stretching, respectively [42]. The hybrid sample spectrum exhibits peaks at 2947 cm^{-1} and 1718 cm^{-1}, which correspond to similar occurrences in the polymer chain. Thus, it can be concluded that the surface characterization technique mainly detects PCL on the surface due to the successful encapsulation of TH within the fibres.

EDX analysis was performed on the hybrid parallel sample to determine the elemental composition of the fibers and the distribution of TH dispersed within the polymer. Fig. 3(b) shows the elemental mapping of carbon, oxygen, nitrogen, and chlorine. The fibres exhibit a significant presence of carbon and oxygen, representing the hydrocarbon chain of PCL with the chemical formula $(C_6H_{10}O_2)n$ [43]. Since PCL constitutes the major component of the electrospinning solution during the fabrication process, it is likely that carbon and oxygen are primarily expressed on the fibre surface. The mapping of carbon and oxygen on the surface indicates the areas where the fibres are deposited and illustrates the dispersion of tetracycline hydrochloride throughout. In contrast, nitrogen and chlorine are present in smaller quantities due to the minimal amount of TH in the electrospun fibres. Nitrogen and chlorine are elements found in the chemical formula of TH, C22H24N2O8.HCl [44]. The drug contained within the aligned fibres appears to be uniformly distributed, as it can be observed in the same quantity across the entire mapping image in the hybrid structure.

3.6. WCA and tensile testing

The water contact angle (WCA) test was performed on the hybrid 3D printed structure to evaluate its hydrophilicity. Previous studies reported that the 3D printed sample alone exhibited an average water contact angle of 104.6°, indicating hydrophobicity caused by the presence of the hydrophobic polymer PCL [24]. However, when fibres were in situ added to the substrate, the water contact angle analysis demonstrated a change in surface hydrophilicity, as shown in Fig. 4(a). All three samples exhibited lower water contact angles, indicating increased hydrophilicity compared to the substrate without fibres. The contact angles measured were 95.3°, 96.6°, and 75° for the parallel, square bracket, and circular geometries, respectively. Since TH is a hydrophilic drug, any surface loading of the drug onto the fibres leads to a slight decrease in the water contact angle compared to the substrate without fibres. This result confirms the successful encapsulation of the TH drug within the electrospun fibres, contributing to their hydrophilic properties. However, since the fibres are predominantly composed of PCL, the samples still maintain a hydrophobic nature. This hydrophobic property of PCL is beneficial for applications such as implants, bone tissue engineering, and slow-release drug delivery systems due to its slow degradation behaviour [45]. The circular geometry alignment sample, with a water contact angle of 75°, is determined to be hydrophilic. Although all samples have the same material composition, and therefore, the hydrophilicity is expected to be consistent, the presence of surface roughness resulting from alignment has an impact on surface wetting. The introduction of surface roughness to a hydrophilic material decreases the contact angle, while for a hydrophobic material, it increases the contact angle [46]. The roughness of the fibres associated with the circular geometry alignment is related to the twisting of fibres, and the presence of the hydrophilic drug-loaded fibres leads to a decrease in the contact angle [47].

Tensile testing was conducted on each alignment geometry and the substrate without fibres to assess the mechanical properties of the changing geometry and the influence of fibre addition on the hybrid structure. Fig. 4(b) illustrates that the square bracket electrode exhibited the highest tensile strain of 480%, followed by the parallel geometry at 411%, and closely followed by the circular geometry at 408%. The increased tensile strain in the square bracket electrode can be attributed to the degree of fibre orientation observed in the SEM image shown in Fig. 2(e). Cordin et al. reported that fibres aligned at a 45° angle demonstrated greater tensile strain compared to those aligned in a single direction [48]. Similarly, Huan et al. conducted a study on the effect of aligned fibres on mechanical properties and concluded that aligned fibres increased tensile stress [49,50]. Among the three fibre alignment geometries, the circular electrode exhibited the highest tensile stress with a value of 4.33 MPa, followed by the square bracket at 4.09 MPa, and then the parallel at 3.09 MPa. This is attributed to the twisting of fibres, as observed in the SEM image in Fig. 2, providing greater tensile strength to the hybrid structure. All three fibre geometries examined enhanced the tensile strain of the hybrid structure, with a 61% increase in tensile strain through the addition of fibres in a square bracket

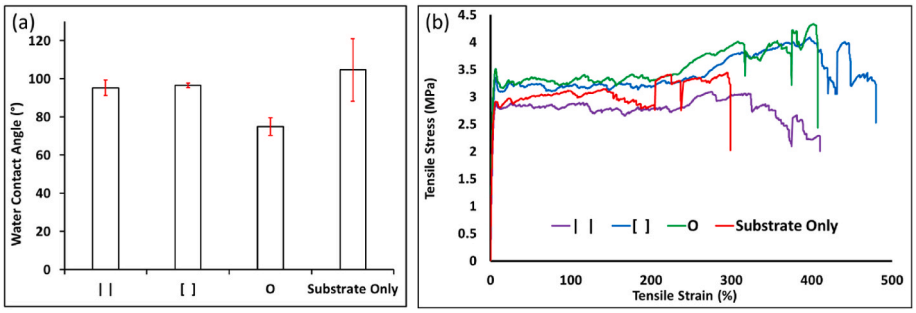

Fig. 4. Water contact angle results (a), and tensile testing of all geometries and substrate only (b).

geometry, and a 26% increase in tensile stress with the addition of fibres in a circular geometry. The tensile stress in the case of circular geometry increases due to the presence of rope-like fibres and their varying degrees of orientation. This enables the structure to withstand a higher stress state, allowing for expansion before failure. However, the arrangement of fibres in a twisted-like configuration may lead to a reduced overall strain in the hybrid structure. Table 1 presents a summary of the tensile stress and strain for all mechanically tested samples. However, the incorporation of fibres has significantly improved the hybrid structure's ability to withstand elongation when exposed to an applied force [51].

3.7. Drug release study

A 10-day study was conducted to evaluate the release of tetracycline hydrochloride (TH) from aligned electrospun fibres, according to previous work [31]. Fig. 5(a) illustrates the sustained release of TH from all alignment geometries. The steady release profiles offer advantages such as reduced side effects associated with high peak drug concentrations and an extended half-life of the drug [52]. Previous alignment methods for electrospun fibres have resulted in initial burst release profiles for polymer fibres loaded with drugs [53]. However, this study circumvents that issue through geometric alignments, leading to sustained drug release. Sustained drug release systems can be categorized as reservoir or matrix systems, which may influence the release kinetics. The encapsulation of the drug plays a significant role in achieving sustained release, typically following a zero-order profile. This type of release system minimizes fluctuations in drug concentrations and reduces the total dosage required [54]. The sustained release profile is influenced by the hydrophobic nature of the hybrid structure, resulting in a single drug release phase through the degradation of PCL. Among the alignment geometries, parallel aligned fibres exhibit the highest amount of drug release, followed by square bracket aligned fibres, and then circular alignment. The orientation of the fibres impacts the drug release profile, with ordered alignment leading to greater release and less ordered alignment resulting in a lower release. The increased sustained release observed in parallel aligned fibres can be attributed to the anisotropic degradation of the aligned fibres [55], as shown in Fig. 2(d), where there is minimal fibre entanglement, allowing for greater surface exposure to the surrounding medium. Fig. 5(b) displays the percentage cumulative release profile corresponding to Fig. 5(a). The linear profiles suggest a zero-order release, which is advantageous in overcoming issues associated with first-order systems as it maintains a constant drug release rate, thereby sustaining the therapeutic window over an extended period [56].

Table 1 presents the mathematical modelling of kinetic drug release profiles for the parallel, square bracket, and circular geometries. Zero order, first order, Korsmeyer-Peppas, Hixson-Crowell, and Higuchi models were applied to calculate the R^2 value by fitting the models to the cumulative percentage drug release data. The zero-order model describes drug release from a system at a constant rate, independent of its concentration, making release solely a function of time [57]. The first-order kinetic model suggests that the rate of concentration variation over time depends on the remaining concentration of the active pharmaceutical ingredient [58]. The Korsmeyer-Peppas model accounts for the combination of multiple diffusion mechanisms, such as Fickian or non-Fickian, in drug release from a polymeric system [59,60]. The

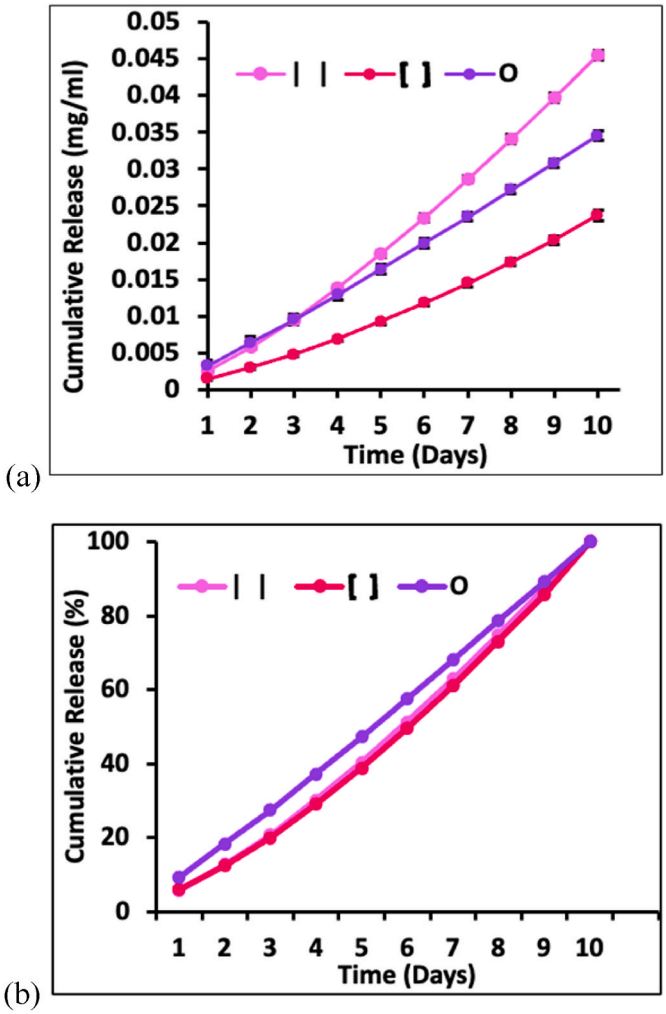

Fig. 5. Cumulative release of tetracycline hydrochloride in mg/ml (a), and percentage cumulative release (%).

Hixson-Crowell model is applied to systems where changes in particle surface area and diameter are expected [61], while the Higuchi model describes the rate of release from matrix devices where the drug loading exceeds the solubility in the medium [62]. Rhine et al. showed the effectiveness of geometric means to achieve zero-order kinetics in matrix delivery systems. All three geometries closely follow a zero-order kinetic release, with the Korsmeyer-Peppas model being the second-best fit, likely due to their matrix-like structure [63]. Based on the R2 values presented in Table 2, it can be concluded that the 3D printed hybrid structure follows the Korsmeyer-Peppas model.

3.8. Thermogravimetric analysis (TGA) and differential scanning colorimetry (DSC)

The thermal degradation behaviour of the hybrid structure, with and without fibres, and the electrospun fibres alone were examined to compare their thermal properties. Fig. 6(a) illustrates a single-stage

Table 1
Tensile stress and strain.

Geometry	Tensile Stress (MPa)	Tensile Strain (%)
| |	3.09	411
[ ]	4.09	480
O	4.33	408
Substrate only	3.44	299

Table 2
Kinetic modelling of drug release.

	Zero order	First order	Korsmeyer-Peppas	Hixson-Crowell	Higuchi
| |	0.9930	0.9189	0.9993	0.9771	0.4739
[ ]	0.9888	0.9343	0.9968	0.9841	0.4715
O	0.9992	0.9176	0.9995	0.9691	0.6330

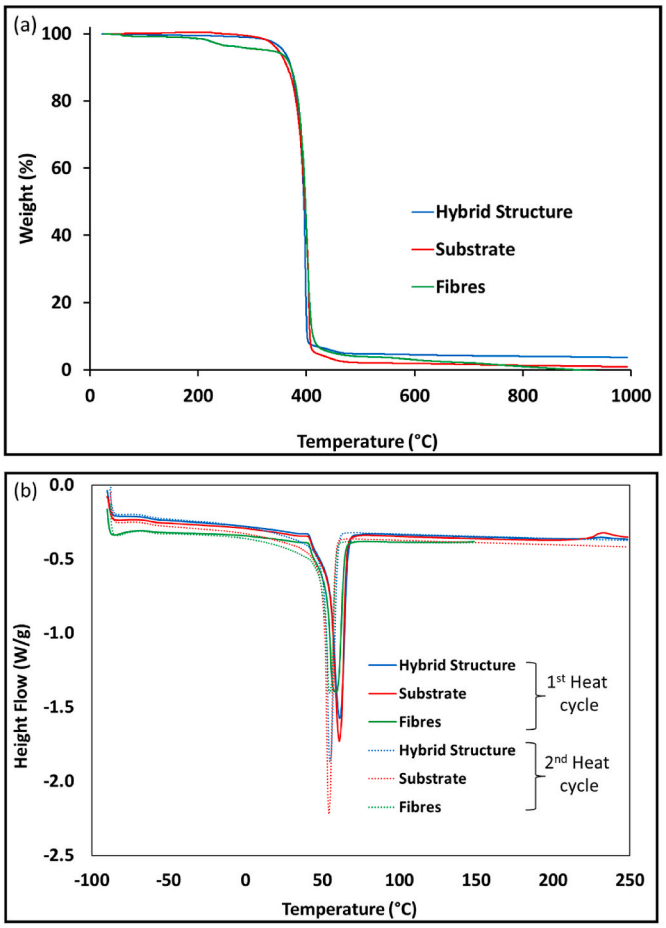

Fig. 6. TGA thermogram (a) and DSC (b) of the hybrid structure, substrate, and fibres.

decomposition process, indicating homogeneous mixing in both manufacturing processes. Significant weight loss is observed at temperatures above 350 °C for the hybrid structure and substrate. This temperature does not conflict with the 130 °C used for hot melt extrusion (HME) of the substrate, suggesting that thermal degradation did not occur during the printing process. Weight loss for the fibres begins at approximately 200 °C, preceding the hybrid structure and substrate. This can be attributed to the presence of trapped solvent within the fibres [64]. However, compared to the hybrid structure and substrate, a significant weight loss of approximately 94% occurs around 350 °C.

Fig. 6(b) displays the first and second heat cycles of the hybrid structure, substrate, and fibres. In contrast to the hybrid structure and substrate, which were heated to 250 °C, the fibre sample was heated only to 150 °C because the TGA analysis in Fig. 6(a) indicated fibre degradation occurring at 200 °C. Therefore, there was no need to test beyond 200 °C. The melting points for the first heat cycle of the hybrid structure, substrate, and fibres were 61.3 °C, 61.0 °C, and 58.7 °C, respectively. Small variations in melting points between all three samples can be attributed to their bulk formation from PCL and the uniform dispersion of materials. The observed peaks display an endothermic reaction, and the melting points align with the literature values for PCL [65]. The slight difference in melting point between samples containing the 3D printed substrate and the fibres may be attributed to the absence of iron oxide nanoparticles. The second heating cycle, represented by the dashed curves in Fig. 6(b), exhibits lower melting points of 54.9 °C, 54.3 °C, and 54.9 °C for the hybrid structure, substrate, and fibres, respectively. This decrease in melting point can be attributed to PCL being a semicrystalline polymer, where the cooling of the material after hot melt extrusion, followed by two additional heat cycles for DSC analysis, can affect the percentage crystallinity within the polymer.

3.9. Simulation

Fig. 7 shows the electric field distribution resulting from the introduction of three designed electrodes using ANSYS simulation. Upon observing the simulation results, it is evident that the shape of the electrodes significantly influences the electric field distribution. When the electric field was maintained between the electrodes and the needle, the parallel electrodes produced the most uniform electric field distribution, while the circular electrodes resulted in the most non-uniform electric field distribution. The electric field distribution of the square bracket template fell between the other two. Under the same simulation conditions, the variation in electrode shape impacted the electric field distribution, ultimately leading to the alignment of fibre distribution. This also explains why PCL fibre deposits at circular electrodes appeared as twisted bundles.

4. Conclusions

A novel combined 3D printing technology was employed to create a hybrid structure featuring in-situ aligned drug-loaded fibres for sustained drug release. The electrospinning setup was modified to include grounded templates with three different design geometries, enabling fibre alignment on a 3D printed substrate produced through hot melt

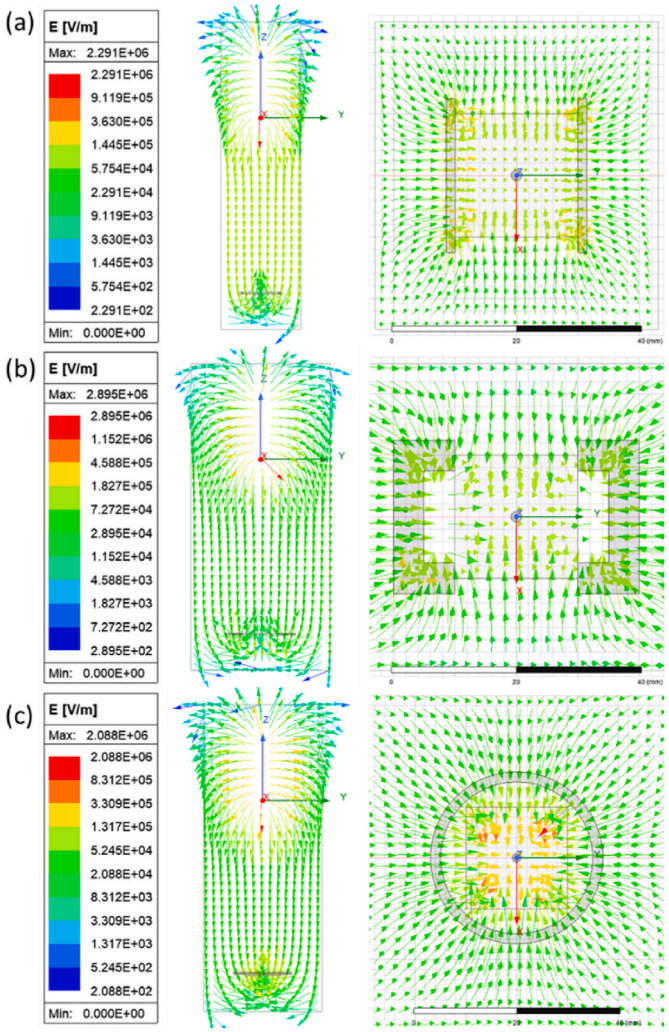

Fig. 7. Electric field simulation of various geometries: (a) parallel electrodes, (b) square bracket electrodes, and (c) circular electrodes.

extrusion. Successful integration of fibres in various orientations was achieved by controlling the electric field using the grounded templates. By adjusting the gap distance of these templates, the micro-scale fibre diameter could be influenced, offering potential applications in additive manufacturing. Elemental characterization confirmed the bulk material as PCL, and effective dispersion of the drug within the fibres was confirmed. The incorporation of in-situ fibres led to enhancements in both the tensile strain and hydrophobicity of the hybrid structure. Furthermore, a 10-day drug release study demonstrated a sustained release profile, showcasing the ability to customize drug release by manipulating the alignment of electrospun fibres to control exposure to the surrounding medium and, consequently, its release properties. Thermal analysis (TGA/DSC) indicated thermal stability surpassing the conditions necessary for 3D printing the hybrid structures. These hybrid structures highlight the successful approach to customizing fibre alignment within printed structures. Furthermore, this technology holds promise for integration into existing printed structures and other biomedical applications, synergistically enhancing their properties and presenting a new approach for advanced therapies, tissue engineering, and personalized medicine.

Author statement

Kirsty Muldoon: Experimentation, data analysis and manuscript writing. Yu Feng, Thomas Dooher & Caolan O'Connor: Experimentation, data analysis and review. Baolin Wang, Hui-Min David Wang, Zeeshan Ahmad and James McLaughlin: Data analysis, discussion and review. Ming-Wei Chang: Conceptualization, supervision and review.

Declaration of competing interest

The authors declare that they have no known competing financial interests or personal relationships that could have appeared to influence the work reported in this paper.

Data availability

Data will be made available on request.

References

[1] P. Mehta, et al., Recent applications of electrical, centrifugal, and pressurised emerging technologies for fibrous structure engineering in drug delivery, regenerative medicine and theranostics, Adv. Drug Deliv. Rev. 175 (2021), 113823.

[2] B. Joshi, et al., Progress and potential of electrospinning-derived substrate-free and binder-free lithium-ion battery electrodes, Chem. Eng. J. 430 (2022), 132876.

[3] K. Muldoon, Y. Song, Z. Ahmad, X. Chen, M.-W. Chang, Micromachines High Precision 3D Printing for Micro to Nano Scale Biomedical and Electronic Devices, 2022, https://doi.org/10.3390/mi13040642.

[4] S.F. Shen, et al., Novel core-shell fiber delivery system for synergistic treatment of cervical cancer, J. Drug Deliv. Sci. Technol. 59 (2020), 101865.

[5] C. Zhang, et al., Nanoporous hollow fibers as a phantom material for the validation of diffusion magnetic resonance imaging, J. Appl. Polym. Sci. 136 (2019), 47617.

[6] Y. Zheng, Fabrication on bioinspired surfaces, Bioinspired Des. Mater. Surfaces (2019) 99–146, https://doi.org/10.1016/B978-0-12-814843-3.00003-X.

[7] J. Xue, T. Wu, Y. Dai, Y. Xia, Electrospinning and electrospun nanofibers: methods, materials, and applications graphical abstract HHS public access, Chem Rev 119 (2019) 5298–5415.

[8] L. Wang, Z. Ahmad, J. Huang, J.S. Li, M.W. Chang, Multi-compartment centrifugal electrospinning based composite fibers, Chem. Eng. J. 330 (2017) 541–549.

[9] I.E. Rebrov, et al., Enhanced electrospinning: multi-level fiber alignment by control of electrohydrodynamic jet motion for tissue engineering, Chem. Eng. J. 418 (2021), 126561.

[10] J. Xie, et al., Aligned-to-random" nanofiber scaffolds for mimicking the structure of the tendon-to-bone insertion site, Nanoscale 2 (2010) 923–926.

[11] M.J. McClure, S.A. Sell, C.E. Ayres, D.G. Simpson, G.L. Bowlin, Electrospinning-aligned and random polydioxanone–polycaprolactone–silk fibroin-blended scaffolds: geometry for a vascular matrix, Biomed. Mater. 4 (2009), 055010.

[12] J.A. Ajao, et al., Electric-magnetic field-induced aligned electrospun poly (ethylene oxide) (PEO) nanofibers, J. Mater. Sci. 45 (2010) 2324–2329.

[13] Y.F. Chang, C.Y. Wu, M.H. Chang, Fabrication of platinum-cobalt nanowires by centrifugal electrospinning as oxygen reduction catalyst for PEMFC, Int. J. Hydrogen Energy (2022), https://doi.org/10.1016/J.IJHYDENE.2022.11.071.

[14] N. Martinez-Prieto, K. Ehmann, Cao, J. Near-field electrospinning on nonconductive substrates using AC fields, Procedia CIRP 93 (2020) 120–124.

[15] D.A. Brennan, K. Shirvani, C.D. Rhoads, S.E. Lofland, V.Z. Beachley, Electrospinning and post-drawn processing effects on the molecular organization and mechanical properties of polyacrylonitrile (PAN) nanofibers, MRS Commun 9 (2019) 764–772.

[16] L. Wang, B. Wang, Z. Ahmad, J.S. Li, M.W. Chang, Dual rotation centrifugal electrospinning: a novel approach to engineer multi-directional and layered fiber composite matrices, Drug Deliv. Transl. Res. 9 (2019) 204–214.

[17] J. Ni, et al., Three-dimensional printing of metals for biomedical applications, Mater. Today Bio 3 (2019), 100024.

[18] M. Tengbo, R. Kunpeng, G. Yongqiang, H. Yixin, G. Junwei, Controlled length and number of thermal conduction pathways for copper wire/poly(lactic acid) composites *via* 3D printing, Sci. China Mater. (2023), https://doi.org/10.1007/s40843-023-2540-9.

[19] T.B. Ma, et al., Thermally conductive poly(lactic acid) composites with superior electromagnetic shielding performances via 3D printing technology, Chinese J. Polym. Sci. (English Ed. 40 (2022) 248–255.

[20] Y. Song, et al., Graphene-based flexible sensors for respiratory and airflow monitoring, ACS Appl. Nano Mater. 6 (2023) 8944.

[21] Y.S. Zhang, et al., 3D extrusion bioprinting, Nat. Rev. Methods Prim. 1 (2021) 75.

[22] G. Liu, M. Hirtz, H. Fuchs, Z. Zheng, Development of dip-pen nanolithography (DPN) and its derivatives, Small 15 (2019).

[23] H.J. Kwon, et al., Overview of recent progress in electrohydrodynamic jet printing in practical printed electronics: focus on the variety of printable materials for each component, Mater. Adv. 2 (2021) 5593–5615.

[24] K. Muldoon, et al., A refined hot melt printing technique with real-time CT imaging capability, Micromachines 13 (2022).

[25] S. Tambe, D. Jain, Y. Agarwal, P. Amin, Hot-melt extrusion: highlighting recent advances in pharmaceutical applications, J. Drug Deliv. Sci. Technol. 63 (2021), 102452.

[26] E. Lenz, K. Löbmann, T. Rades, K. Knop, P. Kleinebudde, Hot melt extrusion and spray drying of Co-amorphous indomethacin-arginine with polymers, J. Pharmaceut. Sci. 106 (2017) 302–312.

[27] S. Bandari, D. Nyavanandi, N. Dumpa, M.A. Repka, Coupling hot melt extrusion and fused deposition modeling: critical properties for successful performance, Adv. Drug Deliv. Rev. 172 (2021) 52–63.

[28] B.C. Palivela, S.D. Bandari, R.S. Mamilla, Extrusion-based 3D printing of bioactive glass scaffolds-process parameters and mechanical properties: a review, Bioprinting 27 (2022), e00219.

[29] C. Tommasino, et al., 3D printed macroporous scaffolds of PCL and inulin-g-P(D,L) LA for bone tissue engineering applications, Int. J. Pharm. 641 (2023), 123093.

[30] I. Koutsamanis, E. Roblegg, M. Spoerk, Controlled delivery via hot-melt extrusion: a focus on non-biodegradable carriers for non-oral applications, J. Drug Deliv. Sci. Technol. 81 (2023), 104289.

[31] P. Karuppuswamy, J. Reddy Venugopal, B. Navaneethan, A. Luwang Laiva, S. Ramakrishna, Polycaprolactone nanofibers for the controlled release of tetracycline hydrochloride, Mater. Lett. 141 (2015) 180–186.

[32] L.F. Zhu, X. Chen, Z. Ahmad, Y. Peng, M.W. Chang, A core–shell multi-drug platform to improve gastrointestinal tract microbial health using 3D printing, Biofabrication 12 (2020), 025026.

[33] I.Y. Wu, S. Bala, N. Škalko-Basnet, M.P. di Cagno, Interpreting non-linear drug diffusion data: utilizing Korsmeyer-Peppas model to study drug release from liposomes, Eur. J. Pharmaceut. Sci. 138 (2019), 105026.

[34] A. Ali, et al., Electrohydrodynamic atomisation driven design and engineering of opportunistic particulate systems for applications in drug delivery, therapeutics and pharmaceutics, Adv. Drug Deliv. Rev. 176 (2021), 113788.

[35] S. Karimi, M.P. Staiger, N. Buunk, A. Fessard, N. Tucker, Uniaxially aligned electrospun fibers for advanced nanocomposites based on a model PVOH-epoxy system, Composer Part A Appl. Sci. Manuf. 81 (2016) 214–221.

[36] C. Peng, et al., Preparation of uniaxially aligned mullite ceramic fibers by electrospinning, Colloids Surfaces A Physicochem. Eng. Asp. 457 (2014) 1–7.

[37] S. Farhaj, B.R. Conway, M.U. Ghori, Nanofibres in drug delivery applications, Fibers 11 (2023), 21 11, 21 (2023).

[38] C. Zhang, C. Gao, M.W. Chang, Z. Ahmad, J.S. Li, Continuous micron-scaled rope engineering using a rotating multi-nozzle electrospinning emitter, Appl. Phys. Lett. 109 (2016), 151903.

[39] X.F. Wu, Y. Salkovskiy, Y.A. Dzenis, Modeling of solvent evaporation from polymer jets in electrospinning, Appl. Phys. Lett. 98 (2011), 223108.

[40] F. Yazdani, B. Fattahi, N. Azizi, Synthesis of functionalized magnetite nanoparticles to use as liver targeting MRI contrast agent, J. Magn. Magn Mater. 406 (2016) 207–211.

[41] M. Lin, et al., Synergistic Effect of Co-delivering Ciprofloxacin and Tetracycline Hydrochloride for Promoted Wound Healing by Utilizing Coaxial PCL/Gelatin Nanofiber Membrane, 2022, https://doi.org/10.3390/ijms23031895.

[42] S. Wu, Z. Ahmad, J.S. Li, M.W. Chang, Fabrication of flexible composite drug films via foldable linkages using electrohydrodynamic printing, Mater. Sci. Eng. C 108 (2020).

[43] M. Singh, R. Singh, M.K. Dhami, Biocompatible thermoplastics as implants/scaffold, Ref. Modul. Mater. Sci. Mater. Eng. (2022) 47–55, https://doi.org/10.1016/B978-0-12-820352-1.00012-2.

[44] I.T. Hameedi, Determination of tetracycline hydrochloride in pure and pharmaceutical samples via oxidative coupling reaction, Mater. Today Proc. 42 (2021) 2953–2958.
[45] C.K. Arakawa, C.A. DeForest, Polymer design and development, Biol. Eng. Stem Cell Niches (2017) 295–314, https://doi.org/10.1016/B978-0-12-802734-9.00019-6.
[46] B.J. Ryan, K.M. Poduska, A. Phys Lett, F. H Wolfs, L. Roughness effects on contact angle measurements, Am. J. Phys. 76 (2008) 1074–1077.
[47] Y. Deng, et al., Recent development of super-wettable materials and their applications in oil-water separation, J. Clean. Prod. 266 (2020), 121624.
[48] M. Cordin, T. Bechtold, T. Pham, Effect of fibre orientation on the mechanical properties of polypropylene–lyocell composites, Cellulose 25 (2018) 7197–7210.
[49] S. Huan, G. Liu, W. Cheng, G. Han, L. Bai, Electrospun Poly(lactic Acid)-Based Fibrous Nanocomposite Reinforced by Cellulose Nanocrystals: Impact of Fiber Uniaxial Alignment on Microstructure and Mechanical Properties, 2018, https://doi.org/10.1021/acs.biomac.8b00023.
[50] M. Yilmaz, N.F. Yilmaz, Effects of raster angle in single- and multi-oriented layers for the production of polyetherimide (PEI/ULTEM 1010) parts with fused deposition modelling, Mater. Test. 64 (2022) 1651–1661.
[51] M.K.R. Aghjeh, M.J. Razavi, Effect of interfibre bonding on mechanical behaviour of electrospun fibrous mats, Mech. Fibrous Networks (2022) 317–354, https://doi.org/10.1016/B978-0-12-822207-2.00007-6.
[52] C. Andrade, Sustained-release, extended-release, and other time-release formulations in neuropsychiatry, J. Clin. Psychiatry 76 (2015) e995–e999.
[53] H. Majd, A. Harker, M. Edirisinghe, M. Parhizkar, Optimised release of tetracycline hydrochloride from core-sheath fibres produced by pressurised gyration, J. Drug Deliv. Sci. Technol. 72 (2022), 103359.
[54] N. Goonoo, et al., Naltrexone: a review of existing sustained drug delivery systems and emerging nano-based systems, J. Contr. Release 183 (2014) 154–166.
[55] M. Eslamian, M. Khorrami, N. Yi, S. Majd, M.R. Abidian, Electrospinning of highly aligned fibers for drug delivery applications, J. Mater. Chem. B 7 (2019) 224.
[56] M.L. Laracuente, M.H. Yu, K.J. McHugh, Zero-order drug delivery: state of the art and future prospects, J. Contr. Release 327 (2020) 834–856.
[57] L. Pourtalebi Jahromi, M. Ghazali, H. Ashrafi, A. Azadi, A comparison of models for the analysis of the kinetics of drug release from PLGA-based nanoparticles, Heliyon 6 (2020).
[58] N.S. Heredia, et al., Comparative statistical analysis of the release kinetics models for nanoprecipitated drug delivery systems based on poly(lactic-co-glycolic acid), PLoS One 17 (2022), e0264825.
[59] R.W. Korsmeyer, R. Gurny, E. Doelker, P. Buri, N.A. Peppas, Mechanisms of solute release from porous hydrophilic polymers, Int. J. Pharm. 15 (1983) 25–35.
[60] L. Ahmed, et al., Study the using of nanoparticles as drug delivery system based on mathematical models for controlled release 8 (2019) 52–56.
[61] F. Rehman, et al., Surface engineered mesoporous silica carriers for the controlled delivery of anticancer drug 5-fluorouracil: computational approach for the drug-carrier interactions using density functional theory, Front. Pharmacol. 14 (2023).
[62] D.R. Paul, Elaborations on the Higuchi model for drug delivery, Int. J. Pharm. 418 (2011) 13–17.
[63] W.D. Rhine, V. Sukhatme, D.S.T. Hsieh, R.S. Langer, A new approach to achieve zero-order release kinetics from diffusion-controlled polymer matrix systems, Control. Release Bioact. Mater. (1980) 177–187, https://doi.org/10.1016/B978-0-12-074450-3.50015-2.
[64] L.F. Zhu, X. Chen, Z. Ahmad, Y. Peng, M.W. Chang, A core–shell multi-drug platform to improve gastrointestinal tract microbial health using 3D printing, Biofabrication 12 (2020), 025026.
[65] M.S. Baburaj, et al., Fabrication and characterisation of polycaprolactone/gelatin/chitosan (PCL/GEL/CHI) electrospun nano-membranes for wastewater purification, Desalination 563 (2023), 116709.